

Characterization of Protein Aggregated Gold Nanocrystals

Stephen Connolly, S. Nagaraja Rao, and Donald Fitzmaurice*

Department of Chemistry, University College Dublin, Belfield, Dublin 4, Ireland

Received: August 11, 1999; In Final Form: March 6, 2000

This paper describes the preparation of an aqueous dispersion of electrostatically stabilized gold nanocrystals. It also describes the characterization of these nanocrystals by NMR, SAXS, SLS, and TEM prior to and following their modification by chemisorption of 3-mercaptopropionic acid. Using the insights gained, these nanocrystals were subsequently modified by chemisorption and appropriate surface concentration of a disulfide biotin analogue (DSBA). Addition of streptavidin to the DSBA-modified gold dispersion results in the binding of gold nanocrystals to opposite faces of the protein and in the aggregation of the dispersion. The growth kinetics and structure of the resulting aggregates were characterized by UV–visible spectroscopy, DLS, SAXS, and TEM. Some implications of these findings for the assembly of complex nanocrystal architectures in solution are considered.

Introduction

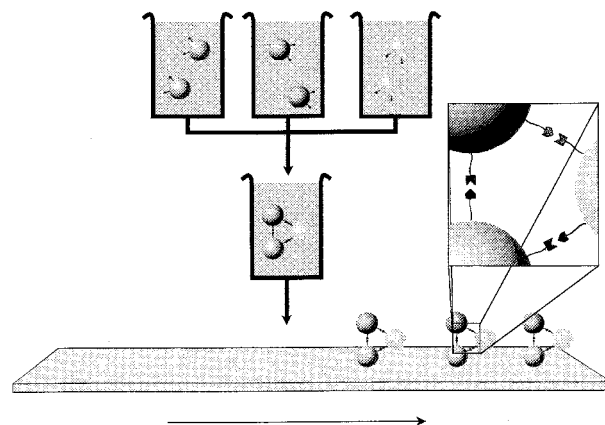
Future growth of the electronics sector will depend on developing faster integrated circuits (ICs) and on reducing costs. In respect of both these objectives, the assembly in solution or at a suitable substrate of complex metal, semiconductor, and insulator nanocrystal architectures is of particular interest.^{1–14} In the medium term, it is expected that such studies will lead to the assembly of arrays of functional nanoscale heterostructures. In the longer term, it is possible such studies will lead to the cost-effective assembly (partial or complete) of ICs capable of processing information at unprecedented speeds.

If, however, these expectations are to be realized, it will be necessary to develop practical strategies for the assembly of complex nanocrystal architectures in solution or at a suitable substrate. One strategy is to adsorb molecules incorporating a binding site at the surface of each nanocrystal of a dispersion. The function of these molecules is to uniquely define the position of a nanocrystal from a given dispersion in the nanocrystal architecture to be assembled. Upon mixing a number of such dispersions, each nanocrystal will recognize and selectively bind a nanocrystal from another dispersion or a well-defined region on a patterned substrate. (Scheme 1) By this means, it will be possible to program the parallel assembly of multiple copies of the desired nanocrystal architecture in solution or at a suitable substrate.

In the present study, we describe the preparation of an aqueous dispersion of electrostatically stabilized gold nanocrystals. The resulting dispersion was characterized by ¹H NMR, static light scattering (SLS), dynamic light scattering (DLS), small-angle X-ray scattering (SAXS), and transmission electron microscopy (TEM).

This dispersion has subsequently been modified by adsorption of a disulfide biotin analogue (DSBA). Addition of streptavidin to the DSBA-modified gold dispersions results in the binding of gold nanocrystals to opposite faces of the protein^{13,15–18} and hence the aggregation of the dispersion (Scheme 2). Similarly, aggregation of the dispersion can be achieved with the reverse order of binding, viz., addition of DSBA to the streptavidin

SCHEME 1 : Biologically Programmed Assembly of Metal, Semiconductor, and Insulator Nanocrystals Leading to a Well-Defined Structure Chemisorbed at a Technologically Relevant Substrate, e.g., a Lithographically Patterned Silicon Wafer



protein results in a complex with disulfide groups on opposite sides of the protein. Addition of this DSBA–streptavidin complex to an unmodified gold nanocrystal dispersion also results in aggregation (Scheme 3). The resulting aggregates were characterized by UV–visible absorption spectroscopy, DLS, SAXS, and TEM.

Experimental Section

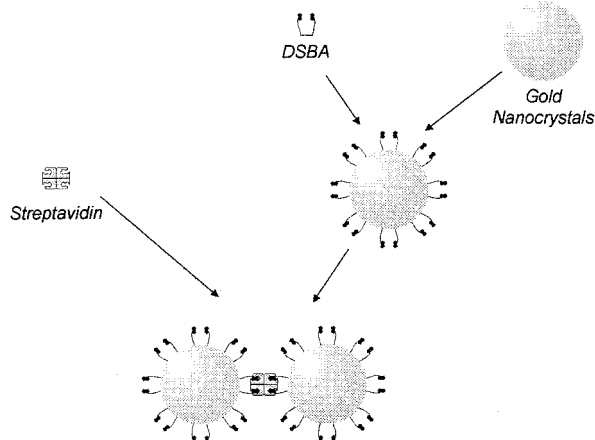
General. All chemicals were used as supplied by the Sigma-Aldrich Chemical Co. Ltd. Distilled deionized Millipore-MilliQ water filtered through a 0.02- μ m inorganic Anotop filter was used to prepare all solutions. Deuterium oxide (99.9 atom % D) was used as supplied from Fluorochem Limited.

Preparation of Disulfide Biotin Analogue. The disulfide biotin analogue was synthesized according to Scheme 4. 1,7-Diaminoheptane (**1**), 3-mercaptopropionic acid (**3**), and D-biotin (**7**) were used as supplied.

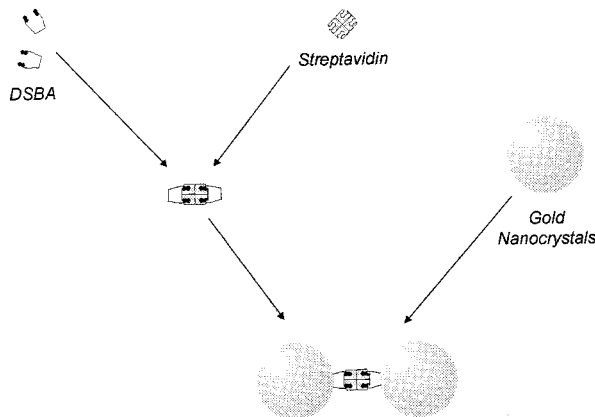
tert-Butyl *N*-(7-aminoheptyl)carbamate (**2**).¹⁹ A solution of di-*tert*-butyl dicarbonate (11.0 mmol, 2.410 g) in dioxane (30

* To whom correspondence should be addressed.

SCHEME 2 : Gold Nanocrystals Are Modified by Chemisorption of DSBA; Subsequent Addition of Streptavidin Is Followed by Binding of the Biotin Moiety in DSBA and Leads to Aggregation of the Dispersion



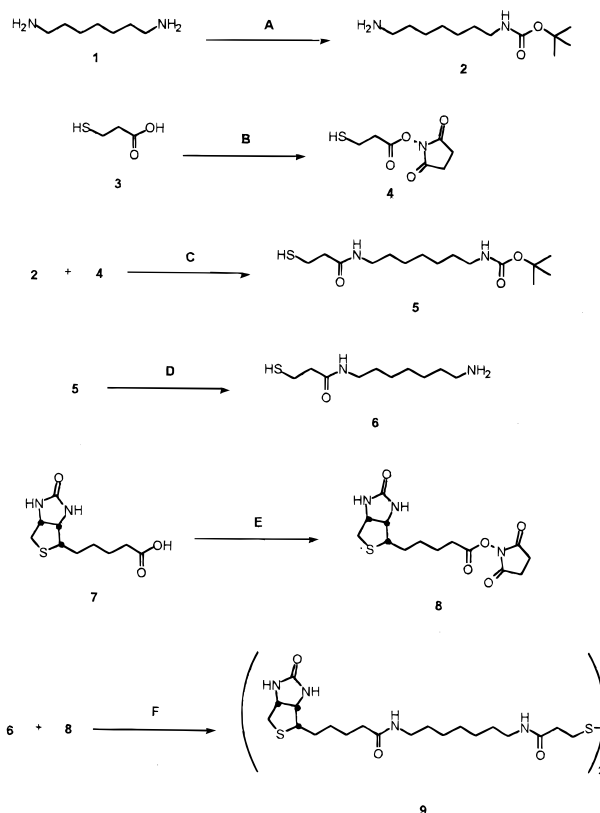
SCHEME 3 : Streptavidin Is Modified by Binding to the Biotin Moiety of DSBA; Subsequent Addition of Gold Nanocrystals Is Followed by Binding of the Streptavidin–DSBA Complex to the Gold Surface, through Chemisorption of the DiSulfide Group of DSBA, and Leads to Aggregation of the Dispersion



mL) was added over a period of 2.5 h to a solution of **1** (87.5 mmol, 11.400 g) in dioxane (30 mL). The mixture was allowed to stir for 22 h, and the solvent was removed under vacuum. Water (50 mL) was added to the residue, and the insoluble bis-substituted product was separated by filtration. The filtrate was extracted with dichloromethane (3 × 50 mL). Unreacted diamine was removed from the dichloromethane extracts by repeated washing with water (6 × 50 mL). The organic phase was dried over anhydrous magnesium sulfate, and the solvent was removed under vacuum to yield 1.28 g of the product, **2**, as a yellow liquid (yield 65% based on di-*tert*-butyl dicarbonate). ¹H NMR (270 MHz, CDCl₃): 1.2–1.5 (m, 22H, CH₂, CH₃, NH₂); 2.6 (t, 2H, *J* = 6.77 Hz, CH₂NH₂); 3.05 (q, 2H, *J* = 6.41, 6.77 Hz, CH₂CH₂NHCOO); 4.6 (s, 1H, CH₂NHCOO).

3-Mercaptopropionyl-N-hydroxysuccinimide Ester (4). N-hydroxysuccinimide (8.7 mmol, 1.00 g) was stirred in dichloromethane (500 mL) over a period of 30 min, yielding a clear solution to which **3** (8.7 mmol, 0.92 g) in dichloromethane (5 mL) was added. 1,3-Dicyclohexylcarbodiimide (9.5 mmol, 1.97 g) in dichloromethane (50 mL) was added dropwise to the reaction mixture over a period of 30 min, and the mixture was then stirred for 24 h. The solid that separated was filtered, and the solvent was removed under reduced pressure to yield 1.725

SCHEME 4 : Synthesis of DSBA



Reagents and Conditions:

- A. (BOC)₂O, 1,4-Dioxane, RT, 24 hr.
 B. N-Hydroxysuccinimide, DCC, CH₂Cl₂, RT, 24 hr.
 C. Et₃N, CHCl₃.
 D. 1) 3 M HCl/MeOH, RT, 30 min 2) Et₃N, CHCl₃, RT, 24 hr.
 E. N-Hydroxysuccinimide, DCC, DMF, RT, 24 hr.
 F. Et₃N, CHCl₃, RT, 168 hr.

g of the product, **4** (yield 97%). ¹H NMR (500 MHz, CDCl₃): δ 1.83 (t, 1H, *J* = 8.79 Hz, -SH); 2.84 (s, 4H, COCH₂CH₂CO); 2.86 (m, 2H, CH₂CH₂SH); 2.95 (t, 2H, *J* = 7.32 Hz, COCH₂-CH₂).

tert-Butyl-N-(7-((3-sulfanylpromyl)amino)heptyl)carbamate (5). To a solution of **2** (2.6 mmol, 0.600 g) and triethylamine (500 μL) in dichloromethane (125 mL), **4** (2.6 mmol, 0.530 g) in dichloromethane (125 mL) was added dropwise over a period of 5 h. The solution was stirred for 24 h at room temperature. The clear dichloromethane solution was washed with water (2 × 125 mL). The dichloromethane layer was dried over anhydrous magnesium sulfate, and the solvent was removed under reduced pressure to yield 0.95 g of the product (**5**) as a yellow waxy solid (yield 65%). ¹H NMR (270 MHz, CDCl₃): 1.3–1.5 (m, 19H, CH₂, CH₃); 1.6 (t, 1H, *J* = 8.79 Hz, SH); 2.45 (t, 2H, *J* = 6.77 Hz, CH₂CH₂CONH); 2.8 (dt, 2H, *J* = 8.42, 6.77 Hz, CH₂CH₂SH); 3.05 (q, 2H, *J* = 6.41 Hz, CH₂CH₂NHCOO); 3.2 (m, CH₂CH₂NHCOCH₂); 4.6 (s, 1H, CH₂NHCOO); 5.6 (s, 1H, CH₂NHCOCH₂).

N-(3-Sulfanylpromyl)diaminoheptane (6). **5** (1.05 mmol, 335 mg) was dissolved in 3 M methanolic HCl (12 mL) and stirred for 30 min at room temperature. The reaction mixture was reduced to dryness on a rotary evaporator. Following the addition of dry triethylamine (2 mL) and dry chloroform (25 mL), the product was used as is in the subsequent reaction.

2,5-Dioxopyrrolidinyl-5-(6,8-diaza-7-oxo-3-thiabicyclo[3.3.0]-oct-2-yl)pentanoate (BNHS) (8). **8** was prepared from **7** according to Bayer & Wilchek²⁰ and was characterized by ¹H NMR.

5-(6,8-Diaza-7-oxo-3-thiabicyclo[3.3.0]oct-2-yl)-N[7-(3-{[2-(N-{7-[5-(6,8-diaza-7-oxo-3-thiabicyclo[3.3.0]oct-2-yl)pentanoylamino]heptyl}carbamoyl)ethyl]disulfanyl}propanoylamino)heptyl]pentanamide (DSBA) (**9**). A solution of **8** (0.525 mmol, 179 mg) in dry chloroform (25 mL) was added dropwise, under nitrogen, to the solution of **6** (0.525 mmol, 115 mg) and triethylamine (100 μ L) in chloroform (25 mL) over the course of 1 h. The reaction mixture was stirred at room temperature for a further 168 h, and then water was added (50 mL), to yield 50 mg of the product, **9**, as a solid insoluble in both the water and chloroform layers (yield 10%).

NMR analysis showed the presence of a 10% impurity of triethylamine hydrochloride, which could not be removed without decomposition of the desired product **9**. The final structure was confirmed by detailed ^1H and ^{13}C NMR spectroscopy. This impurity was found not to interfere with the aggregation, as addition of a further 10 molar equivalent excess of triethylamine hydrochloride had no experimentally observable effect on aggregation kinetics.

^1H NMR (400 MHz, $\text{CD}_3\text{OD}:\text{CDCl}_3$ as 1:1): 1.3–1.8 (m, 32H, CH_2); 2.18 (t, 4H, $J = 7.52$ Hz, $\text{CH}_2\text{CH}_2\text{CONH}$); 2.51 (t, 4H, $J = 7.53$ Hz, $\text{CH}_2\text{CH}_2\text{CONH}$); 2.72 and 2.87 (d and dd, $J = 5.02$, 12.55 Hz, 4H, SCH_2CH); 2.85 (t, 4H, $J = 7.52$ Hz, $\text{CH}_2\text{CH}_2\text{SS}$); 3.13 (m, 2H, SCH); 3.15 (m, 8H, CH_2NHCO); 4.31 and 4.48 (m, 4H, $(\text{CH}_2)_2(\text{NH})_2\text{CO}$).

Satisfactory elemental analyses were obtained for compounds **2**, **4**, **5**, and **8**. **1** and **3** were obtained commercially, and no elemental analyses were performed. The intermediate, **6**, was not isolated, and as a result, no elemental analysis was obtained. The presence of the impurities in the final compound, **9**, prevented satisfactory elemental analysis.

Preparation of Gold Sols. Gold nanocrystal dispersions with narrow size distributions were prepared using the method developed by Frens.²¹ A boiling aqueous solution of hydrogen tetrachloroauric acid trihydrate (250 mL, 0.01% w/v) was reduced by the addition of trisodium citrate (8.75 mL, 1% w/v). After 15 min, the reaction was complete, and the resulting gold sol was allowed to cool to room temperature. The ratio of water to gold salt to citrate controls the relative rates of nucleation and growth and hence the final size of the nanocrystals.

Modification of Gold Sols. Modification of the gold nanocrystals was achieved by addition of a 5-mL aliquot of a 1.55×10^{-6} mol dm^{-3} aqueous solution of DSBA to 50 mL of the gold sol followed by stirring for 30 min.

Preparation of Streptavidin Solutions. Streptavidin was dissolved and dialyzed three times in 0.06 M phosphate buffer, pH 7.5. The activity of the resulting solution was subsequently determined by spectrophotometric titration.²²

Characterization Techniques. *UV-Visible Spectroscopy.* UV-visible spectra were recorded using a Hewlett-Packard 8452A diode array spectrophotometer or an Ocean Optics, Inc. SD2000 fiber optic spectrometer and 10 mm polystyrene fluorimeter cuvette cells supplied by the Sigma-Aldrich Chemical Co.

Nuclear Magnetic Resonance Spectroscopy. 500 MHz NMR spectra were run on a VARIAN UNITY 500 FT spectrometer with ^1H frequency at 499.843 MHz, using standard proton parameters. For the NMR titration experiments, the spectra were recorded at 30 $^\circ\text{C}$ with homonuclear decoupling for D_2O suppression. In each case, to a known mass of the sample at 30 $^\circ\text{C}$, a known mass of the tritrant was added. The solution was then mixed for 1 h before the NMR measurements were taken. These consisted of 1024 scans, corresponding to a total duration of 54 min for each measurement.

400 MHz NMR spectra were run on a Bruker DPX400 spectrometer, with ^1H frequency at 400.14 MHz and ^{13}C at 100.62 MHz. The pulse programs were standard ^1H , ^{13}C , ^{13}C -DEPT, TOCSY, and HMQC routines from the Bruker library. 270 MHz NMR spectra were recorded using a JEOL 270 FT spectrometer with ^1H frequency at 270.05 MHz and standard proton parameters.

270 MHz NMR spectra were used for routine characterization and identification of compounds. 400 MHz NMR spectroscopy was used for the detailed characterization of the final product, **9**, and identification of the impurity (triethylamine hydrochloride). 500 MHz spectroscopy was used for the NMR titration experiments.

Static Light Scattering. Static light scattering at 632.8 nm was performed using a DAWN DSP laser photometer (Wyatt Technology, Inc., Santa Barbara, CA). The laser source was a vertically polarized 5-mW He-Ne laser with an in vacuo wavelength of 632.8 nm operated at a gain of 100. The aqueous nanocrystal dispersion was filtered through 0.02 μm inorganic Anotop filters prior to use. Scattering intensities were measured by fixed detectors at 18 scattering angles from 23 $^\circ$ to 147 $^\circ$ for four dilutions of the aqueous nanocrystal dispersions (average gold nanocrystal concentration,²³ denoted AGNC, in the range 6.7×10^{-10} to 2.5×10^{-9} particle mol dm^{-3} or 0.028 to 0.100 g Au dm^{-3}). Experiments were conducted at room temperature. Ten different scans were averaged for each concentration, with approximately a 45 $^\circ$ rotation of the vial between each scan to average out any scattering artifacts due to vial nonuniformities.

Static light scattering at 488.0 nm was performed using a Malvern PCS-4700 instrument equipped with a 256-channel correlator. The laser source was the 488.0-nm line of a Coherent Innova-70 Ar ion laser, typically at a power of 300 mW. The temperature was maintained at 20 $^\circ\text{C} \pm 0.02$ $^\circ\text{C}$ by an external circulator. The aqueous nanocrystal dispersion was filtered through 0.1 μm inorganic Anotop filters prior to use. Scattering intensities were measured at 10 scattering angles from 30 $^\circ$ to 120 $^\circ$ for five dilutions of the aqueous nanocrystal dispersions (AGNC in the range 6.7×10^{-10} to 2.5×10^{-9} particle mol dm^{-3} or 0.028 to 0.100 g Au dm^{-3}). Ten different scans were averaged for each concentration, with approximately a 45 $^\circ$ rotation of the vial between each scan to average out any scattering artifacts due to vial nonuniformities.

Dynamic Light Scattering. Dynamic light scattering experiments were performed using a Malvern PCS-4700 instrument equipped with a 256-channel correlator. The laser source was the 488.0-nm line of a Coherent Innova-70 Ar ion laser, typically at a power of 20 mW. The temperature was maintained at 20 $^\circ\text{C} \pm 0.02$ $^\circ\text{C}$ by an external circulator. Data treatment was as follows: The scattering intensity autocorrelation function was analyzed using the method of cumulants,²⁴ the first-order cumulant yielding the “z”-average diffusion coefficient, which corresponds to an average hydrodynamic radius. Sample preparation was as follows: All samples were filtered through 0.1 μm sterile Anotop syringe filters. An AGNC of 0.8×10^{-9} particle mol dm^{-3} (0.033 g Au dm^{-3}) was used preparatory experiments having established that absorption effects are negligible at this concentration.

X-ray Scattering. Small-angle X-ray scattering experiments were performed on beam line 8.2 at the Synchrotron Radiation Source (SRS) at the Daresbury Laboratory, Warrington, U.K., using monochromatic radiation of wavelength $\lambda = 1.54$ \AA . The scattering angle was calibrated using an oriented specimen of wet collagen (rat tail tendon). The incident radiation intensity was recorded using a parallel plate ionization detector placed

before the sample cell. Data treatment was as follows: All experimental data were corrected for background scattering, sample absorption, and the positional nonlinearity of the detector. The data were then transformed to yield the pair-distance distribution function using the appropriate Fourier transform.²⁵ The presence of a beam stop results in the loss of information for very low scattering vectors. To minimize truncation effects caused by these missing points, the scattering curve was extrapolated using the Guinier approximation.²⁶ Sample preparation was as follows: All samples were filtered through 0.1 μm sterile Anotop syringe filters. An average gold nanocrystal concentration of 2.5×10^{-9} particle mol dm^{-3} ($0.100 \text{ g Au dm}^{-3}$) was used.

Transmission Electron Microscopy. Transmission electron microscopy was performed on a JEOL JEL-2000 EX electron microscope at an accelerating voltage of 150 keV. Samples were prepared by evaporating a drop of the aqueous dispersion on a carbon-coated copper grid.

All TEM measurements were performed “double blind” in order to eliminate selective sampling and experimenter bias—that is, one of us prepared all the samples (SC), which were then each assigned an individual randomly allocated code, while the other (DF) conducted the measurements; the resulting images were each then assigned a separate randomly allocated code prior to analysis (SC), after which the codes were deciphered.

Theory and Simulation. *General.* The number, weight and z -averages of a property X may be defined for a distribution of particles:

$$\langle X \rangle_n = \frac{\int n(X)X dX}{\int n(X) dX} \quad (1)$$

$$\langle X \rangle_w = \frac{\int w(X)X dX}{\int w(X) dX} \quad (2)$$

$$\langle X \rangle_z = \frac{\int w^2(X)X dX}{\int w^2(X) dX} \quad (3)$$

where $n(X)$ and $w(X)$ are the number and weight distribution functions in terms of the property X . The variance, σ^2 , of any average is

$$\sigma^2 = \langle X^2 \rangle - \langle X \rangle^2 \quad (4)$$

The polydispersity, $W = \langle M \rangle_w / \langle M \rangle_n$, describes the breadth of the distribution of polymer/macromolecular systems, where M is the mass of the polymer/macromolecule. Systems with $Q < 1.05$ can be considered, for most practical purposes, as essentially monodisperse.

In all scattering techniques, a sample scatters a collimated beam of radiation of wavelength λ . The intensity of scattered radiation is measured as a function of scattering angle, θ , normally given in terms of the scattering vector,

$$q = \frac{4\pi\tilde{n}}{\lambda} \sin\left(\frac{\theta}{2}\right) \quad (5)$$

where \tilde{n} is the refractive index of the sample and by convention is taken to be 1 for X-ray and neutron experiments.

X-ray Scattering. In small-angle X-ray scattering, the form factor, $F(q)$, for an isolated homogeneous sphere with a sharp edge is^{27–29}

$$I_{\text{monodisperse}}(q) = F^2(q) = I_e N_e^2 \Phi^2(qr) \quad (6)$$

where $\Phi(x)$ is the particle structure factor, given by eq 7 in terms of the spherical Bessel function j_1 , I_e is the differential cross section for forward scattering from a single electron (a constant), r is the radius of the sphere, and $N_e = \frac{4}{3} \pi r^3 n_e \cdot n_e$ is the excess electron density, that is, the difference between the local electron density and the average electron density of the sample:

$$\Phi_{\text{sphere}}(x) = 3j_1(x) = 3 \frac{\sin(x) - x \cos(x)}{x^3} \quad (7)$$

For a polydisperse sample, we must average the intensity over the particle distribution function:

$$I_{\text{polydisperse}} = \int_0^\infty n(r) I_{\text{monodisperse}}(q, r) dr \quad (8)$$

In principle, one can determine the particle distribution function from the scattered intensity by fitting the experimentally observed scattered intensities to the theoretical scattering intensity; however, there is no unique solution to this problem, and a particular shape to the distribution function must be assumed to fit the data to one or two parameters by minimizing the sum of the squares of the residuals.

An alternative approach is to prepare a Porod plot.³⁰ Substitution of eq 7 into eq 6 and multiplication by q^4 viz.,

$$q^4 I_{\text{monodisperse}}(q) = 16\pi^2 I_e n_e^2 \left[\frac{\sin^2(qr)}{q^2} - \frac{r \sin(2qr)}{q} + r^2 \cos^2(qr) \right] \quad (9)$$

shows that $q^4 I(q)$ is an oscillating function in terms of q . The frequency of oscillations is approximately $2r$ for $qr > 1$ and converges to a limit of $2r$ for $qr \gg 1$. Hence, the radius of the spheres can be determined by plotting the positions of the maxima and minima against their order.

In the case of a polydisperse sample, because the scattered intensity is a z -average of Φ^2 , the radius determined by plotting the positions of the maxima and minima against their order is $\langle r \rangle_z$. Further, the oscillations will be damped at higher q , a consequence of destructive interference. The extent of damping is therefore a measure of the polydispersity of the sample. For a Gaussian (normal) distribution of particles, the amplitude of the oscillations falls as $e^{-2(q\sigma)^2}$.³⁰

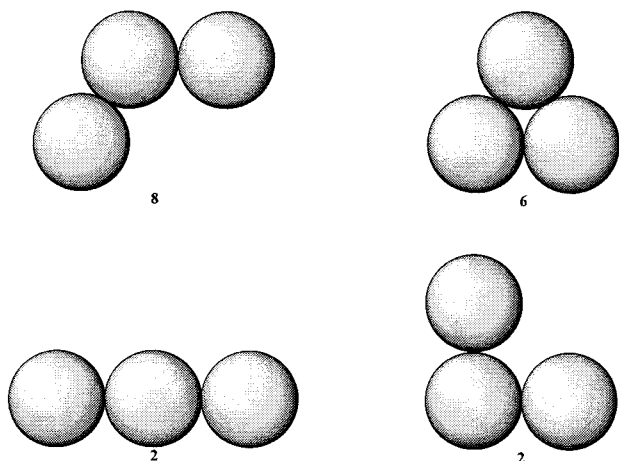
For aggregated samples, there is a further set of oscillations superimposed onto the observed scattering curve (I vs q) due to the spatial relationship between scattering centers. To a first approximation, these oscillations are described by a relationship developed by Debye:^{31,32}

$$I(q) = I_{\text{isolated particle}}(q) \frac{1}{n^2} \sum_{i=1}^n \sum_{j=1}^n \frac{\sin(qr_{ij})}{qr_{ij}} \quad (10)$$

where $I_{\text{isolated particle}}$ is the scattering curve for an isolated particle, n is the number of such particles in the aggregate, and r_{ij} is the distance between particles i and j . This equation yields a reasonable approximation of the scattering of aggregates; however, a more correct description is obtained by modal analysis.^{33,34}

In analyzing the scattering curves of aggregates, it is usually more informative to look at the distance distribution functions derived from the scattering curve. The correlation function $g(r)$

SCHEME 5 : Four Possible Configurations of Trimers, after Rotation into the Plane of the Paper, in an fcc Lattice with Their Corresponding Occurrence Frequencies



describes the probability of finding another particle as a function of separation, r . The pair distance distribution function, $p(r)$, describes the probability of finding two scattering centers separated by a distance r :

$$g(r) = \frac{1}{2\pi} \int_0^\infty I(q) q \frac{\sin(qr)}{r^2} dq \quad (11)$$

$$p(r) = \frac{1}{2\pi} \int_0^\infty I(q) q r \sin(qr) dq \quad (12)$$

When using either of these two equations, it should be noted that, in general, the pair distance distribution function is less susceptible to truncation effects; thus, while interpretation is more involved, the pair distance distribution function is more useful with experimental results.

Computation of Theoretical X-ray Scattering Profiles. The scattering profile of an isolated spherical particle was calculated directly from the square of the form factor for a sphere (eq 7). In the case of a solution of isolated spherical particles, the scattering profile was calculated by integrating the profiles over a Gaussian number distribution with the desired polydispersity (eq 8).

The scattering profile of trimers of spherical particles was calculated from the profile for an isolated sphere using eq 10. To give a more realistic picture, this scattering profile was averaged over several spatial configurations of the trimer. On fixing two spheres at adjacent sites in an fcc lattice—described here normalized, to a sphere radius of $1/2$ and using orthogonal (x, y, z) coordinates (0, 0, 0) and (1, 0, 0)—there remain 18 sites adjacent to an occupied site. These can be reduced by simple rotations to four configurations corresponding to the lattice sites: $(1/2, \sqrt{3}/2, 0) \times 6$; $(-1/2, \sqrt{3}/2, 0) \times 8$; $(-1, 0, 0) \times 2$; and $(0, -\sqrt{3}/3, \sqrt{6}/3) \times 2$. Scheme 5 shows these four configurations after rotation into the xy plane. The scattering profiles of each of these four configurations were calculated and weighted with the corresponding frequencies to yield the theoretical scattering profile of an average trimer.

Static Light Scattering. Static light scattering by a particle suspension is commonly characterized by the Rayleigh ratio R_θ , that is, by the differential scattering cross section per unit volume of suspension at scattering angle θ . The Rayleigh ratio can be calculated from experimentally accessible quantities:³⁵

$$R_\theta = \frac{I_s(\theta)}{I_t(\theta)} \left(\frac{n}{n_t} \right)^2 R_{\theta,t} \quad (13)$$

where $I_s(\theta)$ is the excess scattering intensity of the solute and I_t the scattering intensity of a standard (usually toluene) with a known Rayleigh ratio $R_{\theta,t}$. The square of the ratio of the refractive indices of solvent and scattering standard (n/n_t)² accounts for the corrections of solid angle and scattering volume. For dilute solutions satisfying the Rayleigh–Debye approximation, the theoretical expression for R_θ can be written as the sum of the two terms, that is,³⁶

$$R_\theta = C[\Phi(qr) + Q(q, c)] \quad (14)$$

with q as before and c the weight concentration of the solute. In the simple case of optical uniformity (e.g., homopolymers) and for vertically polarized light, the constant C is given by

$$C = \frac{[2\pi n(dn/dc)]^2}{\lambda^4 N_A} c M_w = K c M_w \quad (15)$$

where (dn/dc) , N_A , and M_w are the refractive index increment of the solute, Avogadro's number, and the weight-average molecular weight of the solute. In the first (self) term of eq 14, the particle scattering factor $\Phi(qr)$ describes the geometrical structure of the solute particles radius r , whereas the second (distinct) term $Q(q, c)$ is also affected by interactions between the particles. For small q and c , $Q(q, c)$ can be expressed in terms of the second virial coefficient A_2 viz., $Q(q, c)_{q,c \rightarrow 0} = -2A_2$.³⁶ Thus, in the dilute regime, we have Zimm's famous formula:^{37,38}

$$\frac{Kc}{R_\theta} = \frac{1}{M_w \Phi(qr)} + 2A_2 c \quad (16)$$

Clearly, the second virial coefficient A_2 contains information about the binary solute interactions. Specifically, positive A_2 indicates that solvent–solute interactions are more favorable than solute–solute interactions. For large positive values of A_2 , the solvent is termed a *good solvent*. $A_2 = 0$ refers to the so-called θ solvent. Negative values of A_2 correspond to the case where solute–solute interactions are favored, that is, phase separation is preferred. Thus, in the case of $A_2 < 0$, we would expect to see aggregation of particles in solution.

Dynamic Light Scattering. For an ideal solution of uniform, noninteracting, rigid, isotropic scatterers, the normalized intensity time correlation function $g^{(2)}(\tau) = \langle I(0)I(\tau) \rangle / \langle I \rangle^2$ obeys the relationship³⁹

$$g^{(2)}(\tau) = 1 + Ae^{-\Gamma\tau} \quad (17)$$

where A is an apparatus-dependent coherence factor, τ the delay time, and Γ the relaxation rate $q^2 D$, D being the translational diffusion coefficient of the solute. For a real system of interacting polydisperse particles, $g^{(2)}(\tau)$ is characterized by a superposition of exponentials with the distribution $f(\Gamma)$ of relaxation rates:

$$g^{(2)}(\tau) = 1 + A \left| \int f(\Gamma) e^{-\Gamma\tau} d\Gamma \right|^2 \quad (18)$$

The technique we use for data analysis is the standard cumulant method.²⁴ Besides the quantity A , we calculate the first two cumulants corresponding to the mean relaxation rate

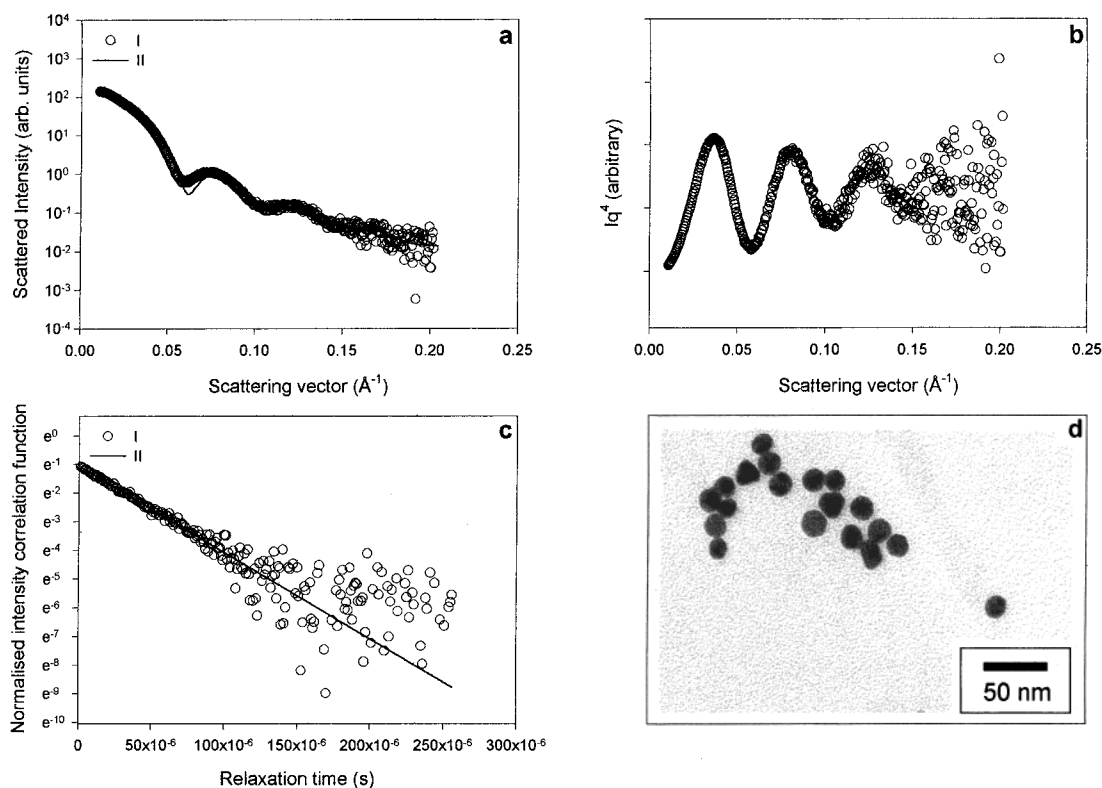


Figure 1. (a) Experimentally determined SAXS scattering intensities for I, a sample of unmodified dispersion of gold nanocrystals (points) and II, theoretical scattering profile calculated for polydisperse nanocrystals of radius $7.1 \pm 0.5 \text{ nm}$ (solid line). (b) Porod plot of experimental data from (a). (c) The normalized intensity correlation function for the same sample as in (a), obtained at 488 nm; cumulant analysis results in a z -average hydrodynamic radius of 9.1 nm. (d) Transmission electron micrograph of particles in (a). Average radius as determined from TEM corresponds to 6.5 nm.

TABLE 1: Average Particle Sizes and Polydispersities as Determined by TEM, SAXS, DLS, and SLS for an Aqueous Dispersion of Unmodified Gold Nanocrystals

| technique | average radius $\langle r \rangle$ (nm) | population standard deviation σ_r (nm) | polydispersity Q |
|-----------|---|---|--------------------|
| TEM | 9.1 ^a | 0.8 | 1.07 |
| SAXS | 7.6 ^b 7.4 ^c | 0.5 | 1.05 |
| DLS | $(8.8 \pm 0.2)^b$ | — ^e | — ^e |
| SLS | $(8.6 \pm 1.9)^d$ | — ^e | — ^e |

^a Number average. ^b z -average. ^c Number average, which for a normal distribution results in the z average observed. ^d Weight average. ^e Analysis used for DLS and SLS yields no information of the population standard deviation and hence polydispersity.

$\langle \Gamma \rangle$ and the variance $\langle \Delta \Gamma^2 \rangle$ from a four-parameter fit of the DLS data.

Results and Discussion

Unmodified Gold Nanocrystals. Colloidal dispersions of gold nanocrystals were among the earliest sols studied; in fact, the preparation used here is a modification of that originally developed by Faraday.⁴⁰ These sols are known to be remarkably stable, with one of Faraday's original sols still existing in a nonaggregated state.⁴¹

Dispersions of unmodified gold nanocrystals were studied using SAXS, DLS, SLS, and TEM. The average sizes of the nanocrystals and, where appropriate, their polydispersities, were determined. Figure 1 shows typical results from these experiments; results are summarized in Table 1. As the different techniques each report a different class of average size, it is to be expected that the sizes will not be directly comparable; however, they are broadly consistent with each other.

In principle, all scattering methods yield an absolute measurement of size. In practice, for reasons discussed in detail below, this is not always the case.

The ability to resolve good data from SAXS relies on the square of the difference in electron density between solvent and the scatterer (see eq 6) and the polydispersity. For gold particles in water, such as those used in this work, the electron density difference is quite high, and the polydispersity is relatively small. Further, since use of SAXS for size determination requires only knowledge of the wavelength of the scattering radiation and the scattering angle, both of which can be determined by geometrical means, size as determined by SAXS can be considered an absolute measurement. These factors support the view that the sizes determined by SAXS are the true sizes of the particles in solution.

For DLS, however, which determines the size through diffusion measurements, the case is quite different. There are two limiting factors: the minimum correlation time and the wavelength of light used. The lower size limit is prescribed by the minimum correlation time, as smaller particles diffuse faster. In this work, the minimum correlation time and the wavelength of light used place a lower limit on determination of the radius at about 2 nm. As the particle size increases toward the wavelength of light, effects due to the angle dependence in the SLS scattering curve tends to reduce confidence in the size returned (while this is not a relevant concern for the isolated nanocrystals, the possibility of such effects must be considered in the case of aggregates of these nanocrystals).

The difference between the radii determined by DLS and SAXS, 91 and 76 Å, respectively, is due to the solvation sphere of the particle. Since DLS determines the diffusion constant of the solvated particle, the radius determined is for the solvated

particle. SAXS, however, returns the radius of the gold core, as solvent scatter is several orders of magnitude less than that of the gold core. The difference between radii determined by DLS and SAXS compares well with that as determined by Wilcoxon et al. for particles of radius 130 Å.⁵¹

The only difference between SLS and SAXS is the wavelength of electromagnetic radiation used. Thus, in principle, SLS should yield a value for the average particle size that is comparable in accuracy to that determined by SAXS. For the wavelengths used in this work, the region of q -space available corresponds to between 0.00009 and 0.00033 Å⁻¹ (eq 5). Given the size of the particles used in this work, the intensity variation expected over this region of q -space corresponds to approximately 0.6% (eqs 7 and 14). The size of the particles must then be determined from variations in this 0.6% variation. Thus, accurate determination of the radius of the scattering particle by SLS is not to be expected. Determination of $\langle M \rangle_w$ from SLS relies on extrapolation to a scattering angle of zero. In the absence of a good estimate for the radius of the scattering particle, such an extrapolation is not feasible.

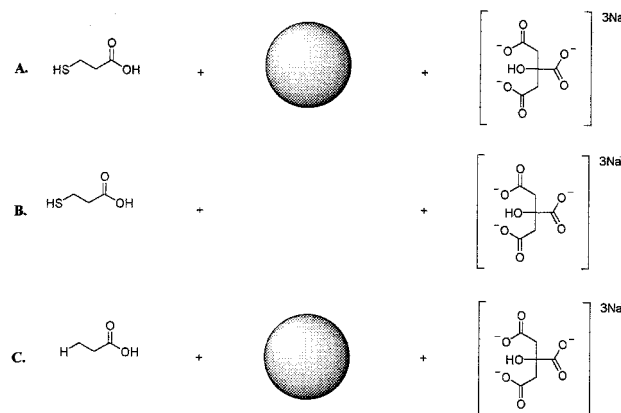
A parameter, which can be determined from SLS, is the second virial coefficient, A_2 . Unlike the radius and weight-average molecular weight, determination of the second virial coefficient is not dependent on the angular variation of the scattered intensity but only on the concentration dependence of the scattered intensity. To determine A_2 reliably, however, the scattered intensity must be extrapolated to zero concentration. Such extrapolation is only valid at concentrations below which only single scattering occurs. For the gold nanocrystals used in this work, the presence of the surface plasmon resonance peak in the UV-visible absorption spectrum complicates this extrapolation, with the result that there is considerable variability in the result. Experimentally, from averaging the results of over 20 determinations at two different wavelengths, we have determined that for this system, A_2 is of the order of $(2 \pm 1) \times 10^{-4}$ mol mL g⁻². This positive value for the second virial, which corresponds to the case where solvation of the nanocrystals is favored over aggregation, is as expected in light of the known stability of such sols.⁴¹

In general, the sizes reported by TEM studies are subject to several sources of variation; for example, by placing the sample on a coated copper grid and evaporating the solvent, we may change the nature of the particles (this is considered unlikely in the case of the gold nanocrystals used here), variations in the beam current can lead to errors as high as 10% in the sizing bar as reported by the TEM instrument (this can be corrected for by the introduction of an external standard), and there is the possibility of selective sampling (can be eliminated by "double-blind" measurements). However, as it is only the absolute and not the relative sizes that are affected, TEM can be quite accurately used to determine sample polydispersity. The polydispersity as determined by TEM compares well with that as determined by SAXS.

Modification of Gold Nanocrystals. It is well established that thiols bind to gold surfaces.⁴²⁻⁴⁵ Furthermore, there are many examples of thiol stabilized organic gold sols.⁴⁶ To the best of our knowledge, however, the only available evidence that thiols bind to the surface of aqueous gold sols has been indirect.⁴⁷ To test this assumption directly, the titration of a thiol against the gold dispersion was carefully followed by NMR.

It has been reported that when thiols bind to gold, the methylene groups α and β to the thiol group are "quenched", either due to broadening to a solidlike structure and/or to shifting from the shielding effects of the metal cluster.⁴⁶ Therefore, by

SCHEME 6 : Three Systems Studied in the NMR Titration: A, Titration of 3-Mercaptopropanoic Acid against the Citrate Stabilized Gold Colloid; B, Titration of 3-Mercaptopropanoic Acid against a Citrate Solution; and C, Titration of Propanoic Acid against the Citrate Stabilized Gold Colloid



using ¹H NMR to monitor the intensity of these resonances as a function of the number of molecules of added thiol, it should be possible to observe the disappearance of the methylene groups α and β to the thiol group on adsorption to the gold surface. In an experiment of this nature, that is, one where the absence of a signal is required, the nature of the controls chosen is of particular importance.

Scheme 6 shows the three systems studied: series A is the experiment, involving addition of 3-mercaptopropanoic acid to a dispersion of gold nanocrystals prepared using the sodium citrate method,²¹ and B and C are both controls, involving, respectively, addition of 3-mercaptopropanoic acid to a solution of sodium citrate and addition of propanoic acid to a dispersion of gold nanocrystals prepared using the sodium citrate method. The results and statistical analyses are shown and summarized, respectively, in Figure 2 and Table 2.

The concentration of compound observed should increase with increasing concentration of compound added. Furthermore, as compound is added to solution, the concentration observed should increase by the amount added, that is, the slope of the graph should be 1. In all three cases (A, B, and C) there was no significant deviation of the slope from 1, that is, the null hypothesis holds.

Assuming that there is no process removing the compound from detection by NMR in solution, the titration should intercept the origin. In the cases of the two control experiments (B and C), the intercept was found to be not significantly different from zero ($P = 0.81$ and 0.98 , respectively), that is, the null hypothesis holds. However, in the case of the experiment (A), the intercept was found to be significantly different from zero ($P < 0.0001$), that is, there is a process which prevents detection of the compound by NMR. Further comparison of the experiment with the controls confirms that the experiment is significantly different from the controls ($P < 0.001$).

As the slope of all three experiments has been confirmed to be 1, a simplified statistical analysis (which should yield a more powerful result), is to compare the average difference between the concentration of compound added and observed, δ . This, as expected, shows that for the experiment, δ is significantly different from 0 ($P = 0.0008$).

The nondetection by NMR of compound only occurs when both thiol and gold are present in solution; hence, it has been directly confirmed that the thiol group is responsible for binding to the gold surface.

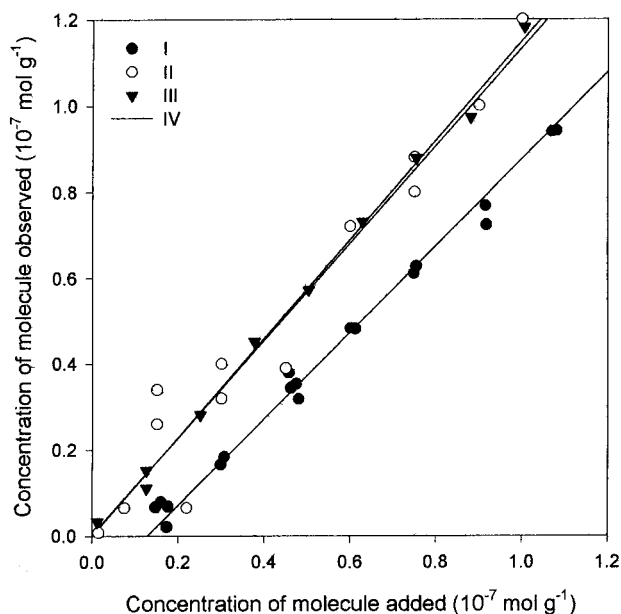


Figure 2. Results of the NMR titrations: I, titration of 3-mercaptopropanoic acid against the citrate stabilized gold colloid; II, titration of 3-mercaptopropanoic acid against a citrate solution; and III, titration of propanoic acid against the citrate stabilized gold colloid.

TABLE 2: Results of Statistical Analysis of the NMR Titration Study: A, Titration of 3-mercaptopropanoic Acid against the Citrate Stabilized Gold Colloid; B, Titration of 3-Mercaptopropanoic Acid against a Citrate Solution; and C, Titration of Propanoic Acid against the Citrate Stabilized Gold Colloid

| | statistic | A | B | C |
|-------------------------------|-------------------------|------------------------|---------------------|----------------------|
| number of samples | <i>n</i> | 19 | 13 | 10 |
| intercept ^a | <i>a</i> | -1.29×10^{-8} | 1×10^{-9} | -3×10^{-11} |
| | <i>s_a</i> | 8×10^{-10} | 4×10^{-9} | 1×10^{-9} |
| | <i>H₀</i> | 0 | 0 | 0 |
| | <i>t</i> | -16.09 | 0.25 | -0.02 |
| | <i>P(H₀)</i> | < 0.0001 | 0.81 | 0.98 |
| slope ^b | <i>b</i> | 1.006 | 1.10 | 1.03 |
| | <i>s_b</i> | 0.004 | 0.08 | 0.02 |
| | <i>H₀</i> | 1 | 1 | 1 |
| | <i>t</i> | 1.37 | 1.29 | 1.53 |
| | <i>P(H₀)</i> | 0.18 | 0.22 | 0.16 |
| added - observed ^c | δ | 1.2×10^{-8} | -6×10^{-9} | -2×10^{-9} |
| | <i>s_δ</i> | 0.3×10^{-9} | 10×10^{-9} | 3×10^{-9} |
| | <i>H₀</i> | 0 | 0 | 0 |
| | <i>t</i> | 3.98 | -0.59 | -0.64 |
| | <i>P(H₀)</i> | 0.0008 | 0.57 | 0.54 |

^a Intercept of linear least-squares analysis. ^b Slope of linear least-squares analysis. ^c δ , average difference between amount added and amount observed.

The difference between the concentration of compound added and observed for the experiment, δ_A , is the molar concentration required for monolayer coverage. Using the average size of the gold nanocrystals as determined by SAXS, the molar surface area of the gold nanocrystals can be calculated. From this and the concentration of particles used, we calculate that monolayer coverage corresponds to a packing density of $18 \text{ \AA}^2/\text{molecule}$. This experimentally determined packing density is somewhat less than the reported packing density required by alkane monolayers on a flat gold surface ($21.4 \text{ \AA}^2/\text{molecule}$).⁴⁸

Aggregation of Unmodified and Modified Gold Nanocrystals. Salt-Induced Aggregation of Unmodified Gold Nanocrystals. Previous work^{49–51} has established that the rapid-

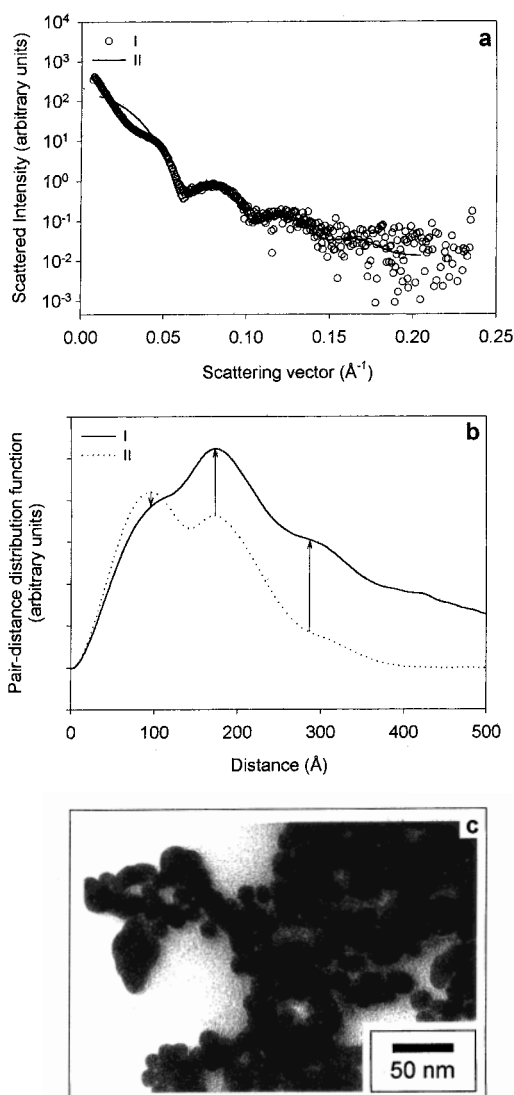


Figure 3. (a) Experimentally determined SAXS scattering intensities for I, a sample of unmodified colloidal gold after aggregation by addition of NaCl (points) and II, theoretical scattering profile calculated for isolated particles of radius 7.5 nm (solid line). (b) Pair distance distribution functions: I, of experimental data from (a) and II, calculated for a ccp lattice averaged trimer of touching spheres ($r = 7.5 \text{ nm}$). (c) Transmission electron micrograph of particles in (a) after the aggregation.

growth kinetics observed with salt (e.g., NaCl) induced aggregation of colloidal gold nanocrystals, as used in this work, is characterized by a power-law dependence of the cluster radius on both sol concentration and time. Both quantities scale with the same growth exponent, 0.38 ± 0.04 . This value precludes simple models of diffusion-limited aggregation as a description of the kinetics, as these predict growth exponents at least as large as 0.7.

Further, DLS and SLS measurements are affected quite strongly by the strong surface plasmon resonance absorption, complicating the analysis of such data. On aggregation, this surface plasmon resonance shifts from 525 to 680 nm, further complicating the analysis. For analysis of the SLS and DLS results of such aggregation, we direct the reader to the excellent work of Wilcoxon et al.⁵¹

To facilitate comparison of SAXS results for salt-induced aggregation with those for streptavidin-induced aggregation, the salt-induced aggregation of colloidal gold nanocrystals has been followed by SAXS.

Figure 3a shows typical results obtained from SAXS. The scattering profile of the aggregates is essentially that of the unaggregated sol at high scattering vectors ($q > 0.05$). This provides evidence that the particles remain as distinct entities, that is, aggregation does not change the nature of the particle. The effects of aggregation become apparent at lower scattering vectors, which is to be expected with an inverse length scale.

To deduce information about the aggregate structure, it is thus useful to transform the data into the PDDF (eq 12). Figure 3b shows the results of this transformation. Comparison of the experimental curve with theoretical calculations for an average trimer of touching hard spheres shows that the peak maxima occur at the same positions. From this fact, we conclude that the particles are touching. TEM of the aggregates, as shown in Figure 3c, also supports the hypotheses that the nanocrystals remain distinct in the aggregate and that the nanocrystals are touching. However, it must be remembered that, in the case of TEM, this is not a true representation of the particles in solution.

Streptavidin-Induced Aggregation of DSBA-Modified Gold Nanocrystals. Chemisorption of DSBA to the surface of gold nanocrystals results in particles primed for aggregation by addition of streptavidin. However, in order for aggregation to occur, the following must be the case: the ratio of biotin groups to binding sites must not be significantly different from 1, as the resultant shortage/excess will serve to halt the aggregation before it becomes significant, and the amount of added streptavidin must not be significantly greater than that required to form a monolayer of binding sites at the surface of the gold nanocrystals, as otherwise negligible aggregation will be observed due to the inaccessibility of the remaining biotin groups.

Thus, the maximum amount of streptavidin is limited by the surface area required for one binding site. As pairs of binding sites exist on opposite faces of the protein, the maximum surface area for a pair of binding sites is 2000 \AA^2 (dimensions of streptavidin $4 \times 4 \times 5 \text{ nm}^{52}$). To achieve optimum aggregation at the corresponding streptavidin concentration, we require a DSBA surface density of $2000 \text{ \AA}^2 \text{ molecule}^{-1}$. In practice, however, due to the random nature of adsorption to the gold surface, at this high concentration of streptavidin not all of the DSBA molecules will be positioned at accessible sites once streptavidin binding becomes significant. For this reason, higher packing densities of DSBA can be used when the streptavidin concentration is close to the limiting concentration.

Gold nanocrystals were modified by addition of DSBA at a surface density of $200 \text{ \AA}^2 \text{ molecule}^{-1}$ this yields a biotin group surface density of $100 \text{ \AA}^2 \text{ molecule}^{-1}$). After modification, the hydrodynamic radius, as determined by DLS, increased from 9.1 to 11.5 nm. The increase of 24 \AA in the hydrodynamic radius is directly comparable with the length of one branch of the DSBA molecule, as computed using simple molecular modeling (24 \AA). The value for the second virial coefficient was not significantly different from that determined for the unmodified nanocrystals. However, it should be noted that the large uncertainty in the second virial coefficient, for both unmodified and modified particles, could hide any change in this parameter due to chemisorption of the DSBA molecule at submonolayer coverage.

Addition of streptavidin, sufficient to result in a surface density of binding groups of $1000 \text{ \AA}^2 \text{ binding group}^{-1}$, resulted in aggregation. The considerable excess surface density of biotin groups relative to the surface density of binding sites can only result in aggregation if the streptavidin surface density is close to monolayer coverage. Addition of streptavidin at higher

concentrations failed to result in aggregation, confirming this hypothesis. Figure 4 shows typical results obtained for aggregation via the route illustrated in Scheme 2.

On addition of streptavidin, DLS shows a power-law dependence of the aggregate size on time. A typical result is shown in Figure 4a. The growth exponent was found to be 0.380 ± 0.007 . This value is similar to those reported from salt-induced aggregation,⁵¹ suggesting that the kinetics for formation of the aggregates is not dissimilar to that involved in salt-induced aggregation. However, again, the presence of the surface plasmon resonance absorption complicates the analysis. Here, this absorption moves from 525 to 546 nm.

Figure 4b shows typical results obtained from SAXS. The scattering profile of the aggregates is, again, essentially that of the unaggregated sol at high scattering vectors ($q > 0.05$). This provides evidence that the particles remain separate, that is, aggregation does not change the nature of the particle. The effects of aggregation, again, become apparent at lower scattering vectors.

Figure 4c shows the results of transformation of the scattering profile into the PDDF (eq 12). Comparison of the experimental curve with theoretical calculations for an average trimer of hard spheres (radius 7.4 nm) separated by 5 nm shows that the peak maxima occur at the same positions. From this fact, we conclude that the particles are separated by approximately 5 nm. It should be noted that streptavidin has dimensions $4 \times 4 \times 5 \text{ nm}$;⁵² thus, we conclude that intercalation of the streptavidin, as expected, is responsible for the separation between the particles.

Figure 4d shows a typical TEM micrograph of a streptavidin-induced aggregation. TEM supports the SAXS data, as in all cases of TEMs, of streptavidin-induced aggregation, no touching particles were observed. In the case of salt-induced aggregation (see above and Figure 3c), one consistently finds touching particles.

DSBA-Streptavidin Induced Aggregation of Unmodified Gold Nanocrystals. By forming the DSBA-streptavidin complex before addition to the gold nanocrystals, it is possible to achieve aggregation due purely to chemisorption of the disulfide to the gold nanocrystal surface. In order for aggregation to occur via this route, the amount of DSBA-streptavidin complex added must be close to that required for monolayer coverage in terms of the DSBA-bound faces of the protein. Significantly lower concentrations will not contain sufficient DSBA-streptavidin complex to induce aggregation, whereas higher concentrations will block aggregation for analogous reasons as the streptavidin induced aggregation of DSBA-modified particles. Figure 5 shows the results of aggregation at a final DSBA surface density of $2000 \text{ \AA}^2 \text{ molecule}^{-1}$.

Again, power law growth is observed (Figure 5a); however, in this case the rate appears to be higher than for streptavidin-induced aggregation of DSBA modified particles, with the growth exponent being 0.45 ± 0.01 . We associate the differences between the kinetics of DSBA-streptavidin induced aggregation of unmodified gold nanocrystals and streptavidin-induced aggregation of DSBA modified gold nanocrystals with the different mechanisms for aggregation. Although the presence of the surface plasmon resonance absorption complicates analysis of the DLS data, this occurs in both cases and can probably be ignored to a first approximation.

DSBA-streptavidin induced aggregation should have relatively low steric hindrance, as one would expect this route to be mediated by S-Au bond formation. Streptavidin-induced aggregation of DSBA-modified gold nanocrystals, on the other hand, relies on binding of biotin by streptavidin. One would

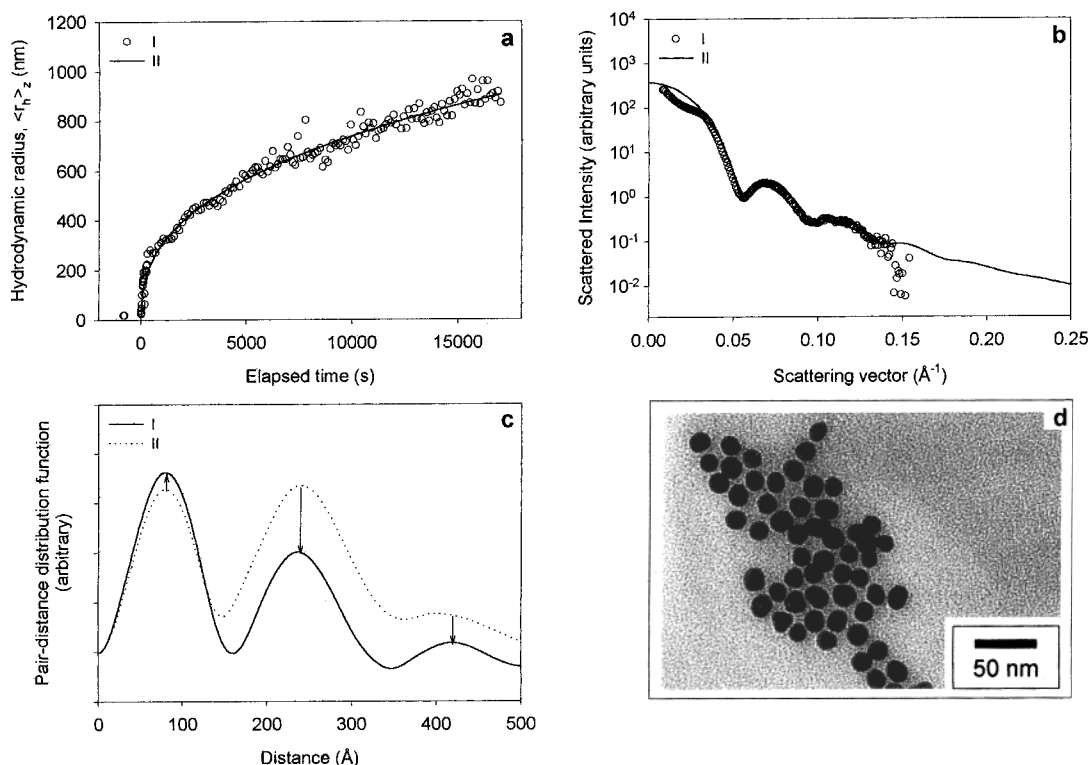


Figure 4. (a) z -Average hydrodynamic radius as a function of time ($t = 0$ corresponds to addition of streptavidin) for I, DSBA modified colloidal gold after addition of streptavidin, obtained at 488 nm, and II, least-squares fit to power-law growth corresponding to $22.4t^{0.38}$. (b) Experimentally determined SAXS scattering intensities for I, a sample of DSBA modified colloidal gold after aggregation by addition of streptavidin (points) and II, theoretical scattering profile calculated for isolated particles of radius 7.4 nm (solid line). (c) Pair distance distribution functions: I, of experimental data from (a) and II, calculated for a ccp lattice averaged trimer of spheres ($r = 7.4$ nm) separated by 4 nm. (d) Transmission electron micrograph of particles in (c) after the average hydrodynamic radius had reached 1400 nm.

expect that binding of biotin by streptavidin would be a sterically more difficult reaction than $S-Au$ bond formation, with a correspondingly slower rate.

Figure 5b shows typical results obtained from SAXS. The scattering profile of the aggregates is, again, essentially that of the unaggregated sol at high scattering vectors ($q > 0.05$). This provides evidence that the particles remain separate, that is, aggregation does not change the nature of the particle. The effects of aggregation, again, become apparent at lower scattering vectors.

Figure 5c shows the results of transformation of the scattering profile into the PDDF (eq 12). Comparison of the experimental curve with theoretical calculations for an average trimer of hard spheres (radius 7.4 nm) separated by 5 nm, again, shows that the peak maxima occur at the same positions. From this fact, we conclude that the particles are separated by approximately 5 nm, and again, we conclude that intercalation of the streptavidin, as expected, is responsible for the separation between the particles.

Figure 5d shows a typical TEM micrograph of a streptavidin-induced aggregation, TEM, again, supporting the SAXS data.

Control Experiments. Several controls have been used to verify that the effects observed are solely due to those attributed. Figure 6 shows the results of monitoring the average aggregate hydrodynamic radius by DLS for these control experiments.

The gold sols are, as expected, stable, with no change in the average hydrodynamic radius observed (I). Addition of the streptavidin buffer solution to the unmodified gold nanocrystals (II) had no effect on the average size as reported by DLS, confirming that the small amounts of ions present in the buffer were insufficient to induce salt induced aggregation.

On addition of DSBA to the unmodified gold nanocrystals (III), as already discussed, the average hydrodynamic radius increases by approximately 24 \AA ; however, no further significant changes are observed over the time scale studied. It should be noted that over the course of several days, the hydrodynamic radius increases; this we attribute to the thioether sulfur group in biotin binding to the gold surfaces. Addition of the streptavidin buffer solution to the DSBA-modified gold nanocrystals (IV) had no effect on the average size as reported by DLS.

Addition of biotin-saturated streptavidin to DSBA-modified gold nanocrystals (V) shows a small increase of the hydrodynamic radius with time, which we attribute to the physisorption of streptavidin at the gold surface and incomplete saturation of the biotin binding sites; however, this is a much slower process than the aggregation phenomena observed in this work.

The results of these control experiments confirm that the gold-sulfur-biotin-streptavidin binding pattern is responsible for the aggregations observed.

Conclusions

An aqueous dispersion of gold nanocrystals possessing a narrow size distribution has been modified by chemisorption of DSBA. Aggregation of these nanocrystals has been induced by addition of streptavidin and followed by DLS, and SAXS and TEM have been used to characterize the structure of the resulting aggregates.

Apart from being one of the first examples of nanocrystal assembly based on protein binding, the significance of these findings is further increased by the fact that there are a large number of biotin analogues with a wide range of rate and equilibrium constants for binding to streptavidin.^{13,18} As a

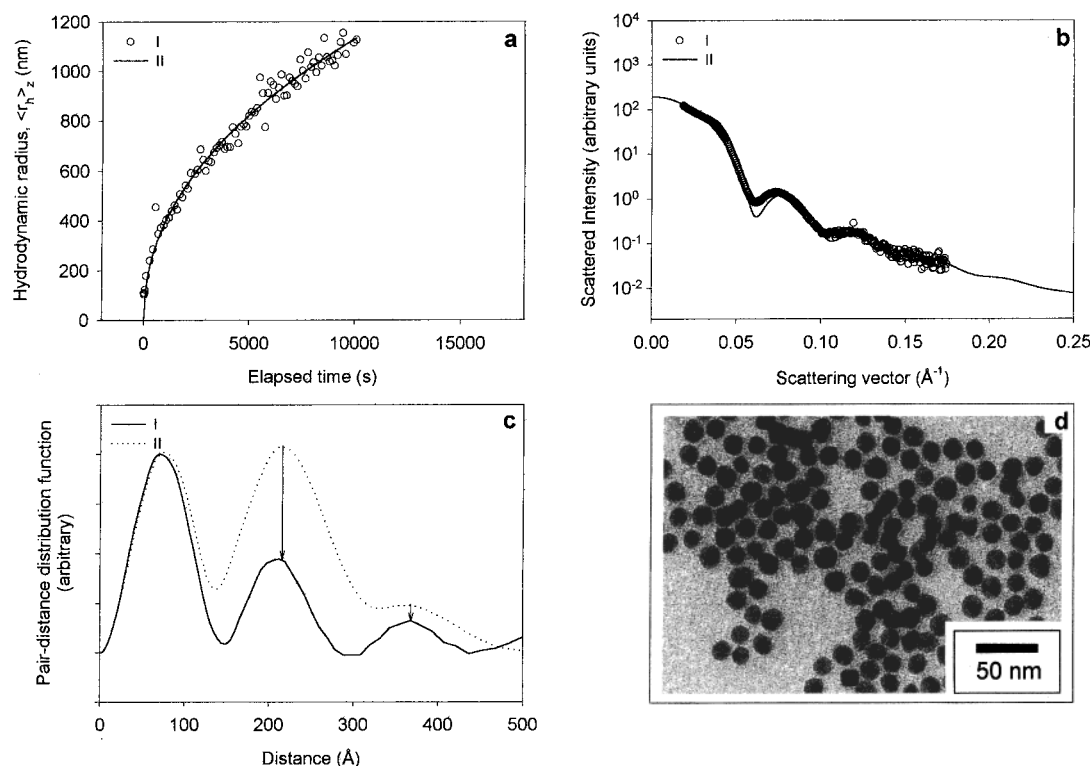


Figure 5. (a) z -Average hydrodynamic radius as a function of time ($t = 0$ corresponds to addition of DSBA₄–streptavidin) for I, unmodified colloidal gold after addition of DSBA₄–streptavidin, obtained at 488 nm and II, least-squares fit to power-law growth corresponding to $17.3t^{0.45}$. (b) Experimentally determined SAXS scattering intensities for I, a sample of unmodified colloidal gold after aggregation by addition of DSBA₄–streptavidin (points) and II, theoretical scattering profile calculated for isolated particles of radius 7.2 nm (solid line). (c) Pair distance distribution functions: I, of experimental data from (a) and II, calculated for a ccp lattice averaged trimer of spheres ($r = 7.4$ nm) separated by 4 nm. (d) Transmission electron micrograph of particles in (c) after the average hydrodynamic radius had reached 1400 nm.

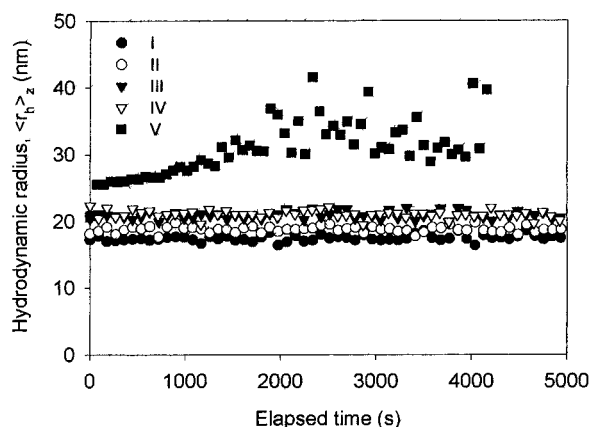


Figure 6. z -Average hydrodynamic radius as a function of time for I, unmodified colloidal gold; II, unmodified colloidal gold on addition of buffer (same concentration as for streptavidin solution); III, unmodified colloidal gold on addition of DSBA, yielding DSBA modified colloidal gold; IV, DSBA modified colloidal gold on addition of buffer (same concentration as for streptavidin solution); and V, DSBA modified colloidal gold on addition of biotin₄–streptavidin.

consequence, the biotin–streptavidin system will prove invaluable in the development and testing of models for nanocrystal assembly in solution or at a substrate and, therefore, in giving practical effect to the strategy outlined in the Introduction. More generally, these findings further support the view that the post-information technologies of the future will emerge at the interface between materials and life sciences.

Acknowledgment. The authors would like to thank Drs. E. Komanschek and N. Teril at the Central Laboratory of the

Research Councils (Daresbury), and Prof. B. Korgel, Dr. H. Rensmo, Dr. N. Zaccheroni, and Mr. S. Fullam at University College Dublin for their assistance in making the reported SAXS measurements at Station 8.2 of the Synchrotron Radiation Source; Profs. I. Stanish and H. Monbouquette at UCLA Chemical Engineering Department for use of their DAWN DSP laser photometer and Prof. B. Korgel for making these measurements; Dr. G. Kelly of the Department of Statistics at University College Dublin for advice on statistical analysis; Dr. J. O'Brien at Trinity College Dublin; and the staff of the NMR and Electron Microscopy Centres both at University College Dublin. We also thank the Commission of the European Union for funding access to the synchrotron radiation source through the Large Scale Facilities Program.

References and Notes

- (1) Xia, Y.; Whitesides, G. M. *Angew. Chem., Int. Ed. Engl.* **1998**, 37, 550.
- (2) Andres, R. P.; Bein, T.; Dorogi, M.; Feng, S.; Henderson, J. I.; Kubiak, C. P.; Mahoney, W.; Osifchin, R. G.; Reifenberger, R. *Science* **1996**, 272, 1323.
- (3) Murray, C. B.; Kagan, C. R.; Bawendi, M. G. *Science* **1995**, 270, 1335.
- (4) Mirkin, C. A.; Letsinger, R. L.; Mucic, R. C.; Storhoff, J. J. *Nature* **1996**, 382, 607.
- (5) Alivisatos, A. P.; Johnsson, K. P.; Peng, X.; Wilson, T. E.; Loweth, C. J.; Bruchez, M. P., Jr.; Schultz, P. G. *Nature* **1996**, 382, 609.
- (6) Lawless, D.; Kapoor, S.; Meisel, D. *J. Phys. Chem.* **1995**, 99, 10329.
- (7) Jordan, C. E.; Frutos, A. G.; Thiel, A. J.; Corn, R. M. *Anal. Chem.* **1997**, 69, 4939.
- (8) Storhoff, J. J.; Elghanian, R.; Mucic, R. C.; Mirkin, C. A.; Letsinger, R. L. *J. Am. Chem. Soc.* **1998**, 120, 1959.
- (9) Braun, E.; Eichen, Y.; Sivan, U.; Ben-Yoseph, G. *Nature* **1998**, 391, 775.
- (10) Shenton, W.; Pum, D.; Sleytr, U. B.; Mann, S. *Nature* **1997**, 389, 585.

- (11) Rao, S. N.; Fitzmaurice, D. *Helv. Chim. Acta* **1998**, *81*, 902.
- (12) Cusack, L.; Rizza, R.; Gorelov, A.; Fitzmaurice, D. *Angew. Chem., Int. Ed. Engl.* **1997**, *36*, 848.
- (13) Green, N. M. *Adv. Protein Chem.* **1975**, *29*, 85.
- (14) Buckland, R. M. *Nature* **1986**, *320*, 557.
- (15) Bayer, E. A.; Wilchek, M. *Anal. Biochem.* **1988**, *171*, 1.
- (16) Blankenburg, R.; Meller, P.; Ringsdorf, H.; Salesse, C. *Biochemistry* **1989**, *28*, 8214.
- (17) Häussling, L.; Michel, B.; Ringsdorf, H.; Rohrer, H. *Angew. Chem., Int. Ed. Engl.* **1991**, *30*, 569.
- (18) Hoffmann, M.; Müller, W.; Ringsdorf, H.; Rourke, A. M.; Rump, E.; Suci, P. A. *Thin Solid Films* **1992**, *210/211*, 780.
- (19) Krapcho, A. P.; Keull, C. S. *Synth. Commun.* **1990**, *20*, 2559.
- (20) Bayer, E.; Wilchek, M. *Methods Enzymol.* **1970**, *18A*, 265.
- (21) Frens, G. *Nature (London) Phys. Sci.* **1973**, *241*, 20.
- (22) Green, N. M. *Methods Enzymol.* **1970**, *18A*, 418.
- (23) Particle concentrations were calculated by assuming that all the gold was reduced to form gold nanocrystals; that the density of the gold nanocrystals is the same as for bulk gold; and that the particles were monodisperse, with a radius of 7.4 nm. This corresponds to a particle mass of 2.0×10^7 g mol⁻¹.
- (24) Koppel, D. E. *J. Chem. Phys.* **1972**, *57*, 4814.
- (25) Glatter, O. In *Neutron, X-Ray and Light Scattering*; Lindner, P., Zemb, Th., Eds; North-Holland: Amsterdam, 1991; pp 33–82.
- (26) Cotton, J. P.; In *Neutron, X-Ray and Light Scattering*; Lindner, P., Zemb, Th., Eds; North-Holland: Amsterdam, 1991; pp 19–31.
- (27) Glatter, O.; Kratky, O. *Small-Angle X-ray Scattering*; Academic Press, Inc: London, 1982.
- (28) Guinier, A. *Small-Angle Scattering of X-rays*; Wiley: New York, 1955.
- (29) *Neutron, X-Ray and Light Scattering*; Lindner, P., Ed.; North-Holland: Amsterdam, 1991.
- (30) Megens, M.; van Kats, C. M.; Bösecke, P.; Vos, W. L. *Langmuir* **1997**, *13*, 6120–6129.
- (31) Debye, P. *Ann. Phys. (Leipzig)* **1915**, 809.
- (32) Debye, P. *Physik. Zeitschr.* **1930**, *31*, 419.
- (33) Holthoff, H.; Borkovec, M.; Schurtenberger, P. *Phys. Rev. E* **1997**, *56*, 6945.
- (34) Mackowski, D. W. *Proc. R. Soc. London A* **1991**, *433*, 599.
- (35) Bantle, S.; Schmidt, M.; Burchard, W. *Macromolecules* **1982**, *15*, 1604.
- (36) Yamakawa, H. *Modern Theory of Polymer Solutions*; Harper and Row: New York, 1971.
- (37) Zimm, B. H. *J. Chem. Phys.* **1948**, *16*, 1099.
- (38) This formula results after application of a binomial expansion.
- (39) Berne, B.; Pecora, R. *Dynamic Light Scattering*; Wiley and Sons: New York, 1976.
- (40) Faraday, M. *Philos. Trans. R. Soc. London, Ser. A* **1857**, *147*, 145.
- (41) Handley, D. In *Colloidal Gold: Principles, Methods, and Applications*; Hayat, M. A., Ed.; Academic Press: San Diego, CA, 1989; Vol. 1, pp 1–12.
- (42) Dubois, L. H.; Nuzzo, R. G. *Annu. Rev. Phys. Chem.* **1992**, *43*, 437.
- (43) Bain, C. D.; Evall, J.; Whitesides, G. M. *J. Am. Chem. Soc.* **1989**, *111*, 7155.
- (44) Bain, C. D.; Evall, J.; Whitesides, G. M. *J. Am. Chem. Soc.* **1989**, *111*, 7164.
- (45) Atre, S. V.; Leidberg, B.; Allara, D. L. *Langmuir* **1995**, *11*, 3882.
- (46) Badia, A.; Gao, W.; Singh, S.; Demers, L.; Cuccia, L.; Reven, L. *Langmuir* **1996**, *12*, 1262.
- (47) Weisbecker, C. S.; Merritt, M. V.; Whitesides, G. M. *Langmuir* **1996**, *12*, 3763.
- (48) Strong, L.; Whitesides, G. M. *Langmuir* **1988**, *4*, 546.
- (49) Weitz, D. A.; Oliveria, M. *Phys. Rev. Lett.* **1984**, *52*, 1433.
- (50) Weitz, D. A.; Lin, M. Y.; Sandroff, C. J. *Surf. Sci.* **1985**, *158*, 147.
- (51) Wilcoxon, J. P.; Martin, J. E.; Schaefer, D. W. *Phys. Rev. A* **1989**, *39*, 2675.
- (52) Weber, P. C.; Ohlendorf, D. H.; Wendoloski, J. J.; Salemme, F. R. *Science (Washington, DC)* **1989**, *243*, 85.